

Enhanced chromospheric 3-minute oscillatory power associated with the 2011-February-15 X2.2 flare

LAUREL FARRIS¹ AND R. T. JAMES MCATEER¹

¹*New Mexico State University*

ABSTRACT

The origin of the 3-minute oscillations of the chromosphere has been attributed to both slow magnetohydrodynamic waves propagating from the photosphere, and to oscillations generated within the chromosphere itself at its natural frequency as a response to a disturbance. Here we present an investigation of the spatial and temporal behavior of the chromospheric 3-minute oscillations before, during, and after the SOL2011-02-15T01:56 X2.2 flare. Ultraviolet emission at 1600 and 1700 Angstroms obtained at 24-second cadence from the Atmospheric Imaging Assembly on board the Solar Dynamics Observatory was used to create power maps as functions of both space and time. A Fourier transform was applied to the intensity signal from individual pixels starting at each observation time over time segments 64 frames (25.6 minutes) in length. We detect an increase in the 3-minute power during the X-class flare, as well as during other smaller events before and after the flare. The enhancement is concentrated in small areas, supporting the injection of energy by nonthermal particles. The potential correlation between 3-minute power and magnetic field strength is discussed, along with formation height dependencies.

Keywords: chromosphere, flares, oscillations

1. INTRODUCTION

Most of the radiative energy associated with solar flares is emitted from the chromosphere in the form of optical and UV emission, but the mechanism of energy transport from the magnetic reconnection site to the chromosphere and subsequent conversion to other forms remains unclear. The chromosphere has been observed to oscillate in response to an injection of energy, suggesting that the nature of such oscillations may reveal something about the nature of energy deposition and conversion associated with flares. In this paper, we aim to characterize the oscillatory response of the chromosphere before, during, and after an X-class flare with the goal of further investigating the “flaring chromosphere” and helping to constrain the origin of the persistent 3-minute oscillations in the chromosphere.

Embedded within the large-scale variations in a typical flare lightcurve are temporal fluctuations known as quasi-periodic pulsations (QPPs). Typical oscillation periods of QPPs range from ~ 1 second to several minutes, and have been observed throughout the duration of solar flares in all wavelength bands. QPPs are considered to be an intrinsic property of flares, thereby providing an observable probe into the reconnection site and surrounding plasma (Inglis et al. 2015). There are two prevailing theories explaining the mechanism that generates QPPs. One theory is that they reflect the energy deposition rate via non-thermal particles accelerated periodically by magnetic reconnection. The second theory is that they are observational signatures of MHD waves

induced in the plasma near the reconnection site, by either magnetic reconnection itself or the mechanism that triggered the onset of reconnection (Nakariakov & Melnikov 2009). QPPs in thermal emission provides insight into the transportation and conversion of energy in the chromosphere during flares.

The dominant power at the 3-minute period in the chromosphere has been attributed to the acoustic cut-off frequency at the base of the chromosphere, $\nu_0 \approx 5.6$ mHz, which corresponds to a period around 3 minutes. This effectively creates a barrier across which waves can travel only if their propagation frequency is higher than ν_0 . Another theory attributes these oscillations to the response of the chromospheric plasma to disturbances at its own natural frequency. This was predicted and shown numerically by a series of papers by Sutmann & Ulmschneider (1995a,b); Sutmann et al. (1998), and other studies by Chae & Goode (2015). Sych et al. (2009) suggested that the leakage of umbral 3-minute oscillations into the upper atmosphere was the cause of flaring QPPs, supported by observations of a similar periodicity in the flare emission. Using Dopplergrams from MDI on SOHO, covering several X-class flares, Kumar & Ravindra (2006) found enhancements of the 3-minute oscillations in velocity that preceded the GOES peak time of the flares. These enhancements were locally concentrated around regions that produced hard X-ray emission, indicating that the enhancement was caused by energetic non-thermal particles. Brosius & Daw (2015) studied UV stare spectra of an M-class flare in Si IV, C I, and O IV lines, and reported four complete

intensity fluctuations with periods around 171 seconds. Their results showing periodic brightenings supported the model of non-thermal particle beams injecting the chromosphere with energy. Kwak et al. (2016) observed the response of the chromosphere to a downflow event using high-resolution spectra from the *Interface Region Imaging Spectrograph (IRIS; De Pontieu et al. (2014))*.

Milligan et al. (2017) observed an enhancement in the 3-minute power from thermal emission that was not present in X-ray emission associated with the flare, supporting the prediction that the chromosphere naturally responds to an impulsive disturbance at the acoustic cutoff frequency.

Monsue et al. (2016) observed an enhancement of frequencies between 1 and 8 mHz associated with an M- and X-class flare in H α emission integrated over the AR, but investigation of subregions revealed an enhancement at low frequencies (1-2 mHz) in inner flare regions before and after the flare, and a suppression of oscillatory power over all frequencies between 1 and 8 mHz during the main phases.

Awasthi et al. (2018) found two distinct pre-flare phases, beginning with non-thermal particles and evolving into a thermal conduction front. Fletcher et al. (2013) studied both the thermal and non-thermal response of the chromosphere during the early stages of an M-class flare, and found the main flux to originate from a different location from the initial brightenings.

The goal of the present study is to investigate the location of power enhancement before, during, and after a flare. The extra time will allow comparison between flaring and non-flaring chromosphere to distinguish whether the plasma is oscillating at the natural frequency of the chromosphere or responding to an impulsive injection of energy. The location of power enhancement will help probe the nature of the energy deposition at various phases.

Here we present the spatial and temporal evolution of 3-minute power in the chromosphere during the *GOES* X-class flare that occurred on 15 February 2011. The Atmospheric Imaging Assembly (AIA; Lemen et al. (2012)) on board the *Solar Dynamics Observatory* (SDO; Pesnell et al. (2012)) provides images with a spatial size scale of 0.6" per pixel and 24-second cadence in thermal UV emission from two channels that sample the lower atmosphere. These data allow the computation of spatially resolved power maps centered on the frequency of interest. The flare, data, and methodology are described in §2. Results are presented and interpreted in §4. Discussion of results, including potential relationship between oscillations and magnetic field is in §5. Conclusions and proposed future work are discussed in §6.

2. OBSERVATIONS AND DATA REDUCTION

The 2011 February 15 X2.2 flare occurred in NOAA active region (AR) 11158 close to disk center during solar cycle 24 (SOL2011-02-15T01:56). The AR was composed of a quadrupole: two sunspot pairs (four sunspots total). The X-flare occurred in a delta-spot composed of the leading spot of the southern pair and the trailing spot of the northern pair. It started at 01:44UT, peaked at 01:56UT, and ended at 02:06UT, as determined by the soft X-ray flux from the *Geostationary Operational Environmental Satellite* (*GOES*-15; [Viereck et al. \(2007\)](#)). The impulsive phase lasted about 10 minutes. Data covering 5 hours centered on this flare were used for the analysis. This data includes a C-class flare that occurred between 00:30 and 00:45 UT on 15 February 2011.

SDO/AIA obtains full disk images [throughout](#) the solar atmosphere, using narrow band filters centered on 10 different wavelengths, two of which provide measurements of thermal UV emission from the [chromosphere](#). The 1700Å channel [mostly contains](#) continuum emission from the temperature minimum, and the 1600Å channel [covers](#) both continuum emission and the C IV spectral line in the upper photosphere and transition region. Both channels have a cadence of 24 seconds and [spatial size scale](#) of 0.6 arcseconds per pixel.

Data from the Helioseismic and Magnetic Imager (HMI; [Scherrer et al. \(2012\)](#)), also on board *SDO*, is used to [study](#) potential correlations between magnetic field strength and oscillatory behavior in the chromosphere. HMI obtains full disk data in the form of line-of-sight magnetograms, vector magnetograms, Doppler velocity, and continuum intensity, measured at the Fe I absorption line at 6173Å with a passband width of 0.076Å. Each [data product](#) has a cadence of 45 seconds (with the exception of the vector magnetograms, at 135 seconds), and [spatial size scale](#) of 0.5 arcseconds per pixel ([Schou et al. 2012](#)).

The standard data reduction routine *aia_prep.pro* from solarsoft was [applied to all data](#).

Figure 1 shows light curves for the full 5-hour time series from 00:00 to 04:59 on 2011-February-15. The top panel shows both AIA channels. The bottom panel shows both SXR channels from *GOES*-15 at 1-8Å (black curve) and 0.5-4Å (pink curve). A small C-flare occurred before the X-flare between 00:30 and 00:45 UT, and two small events occurred after the X-flare, between 03:00 and 03:15, and between 04:25 and 04:45.

Pre-flare images of the full disk are shown in Figure 2, along with a 300x198 arcsecond subset of the data centered on AR 11158. [This subset was extracted and aligned by cross correlation](#) ([McAteer et al. 2003, 2004](#)). Images were scaled to improve contrast using the *aia_intscale.pro* routine from *sswidl*. The magnetic configuration of the quadrupole is clear in the HMI magnetograms. The northern pair will be designated

as AR_1 and the southern pair will be designated as AR_2. Sunspots in the northern pair will be designated as AR_1a (positive polarity) and AR_1b (negative polarity). Sunspots in the southern pair will be designated as AR_2a (positive polarity) and AR_2b (negative polarity).

Both AIA channels saturated (≥ 15000 counts) in the center during the peak of the X-class flare, and a few pixels also saturated during the smaller events before and after. Affected pixels were [all](#) contained within the 300x198 arcsecond [subset of data](#) throughout the duration of the time series. Four images from the 1700Å channel on AIA were missing, between the images with start times at 00:59:53.12, 01:59:29.12, 02:59:05.12, and 03:58:41.12, and the following images, each with start times 48 seconds after the previous image. Since the gaps in data were separated by an hour, it was reasonable to approximate [missing images](#) by averaging the two adjacent images.

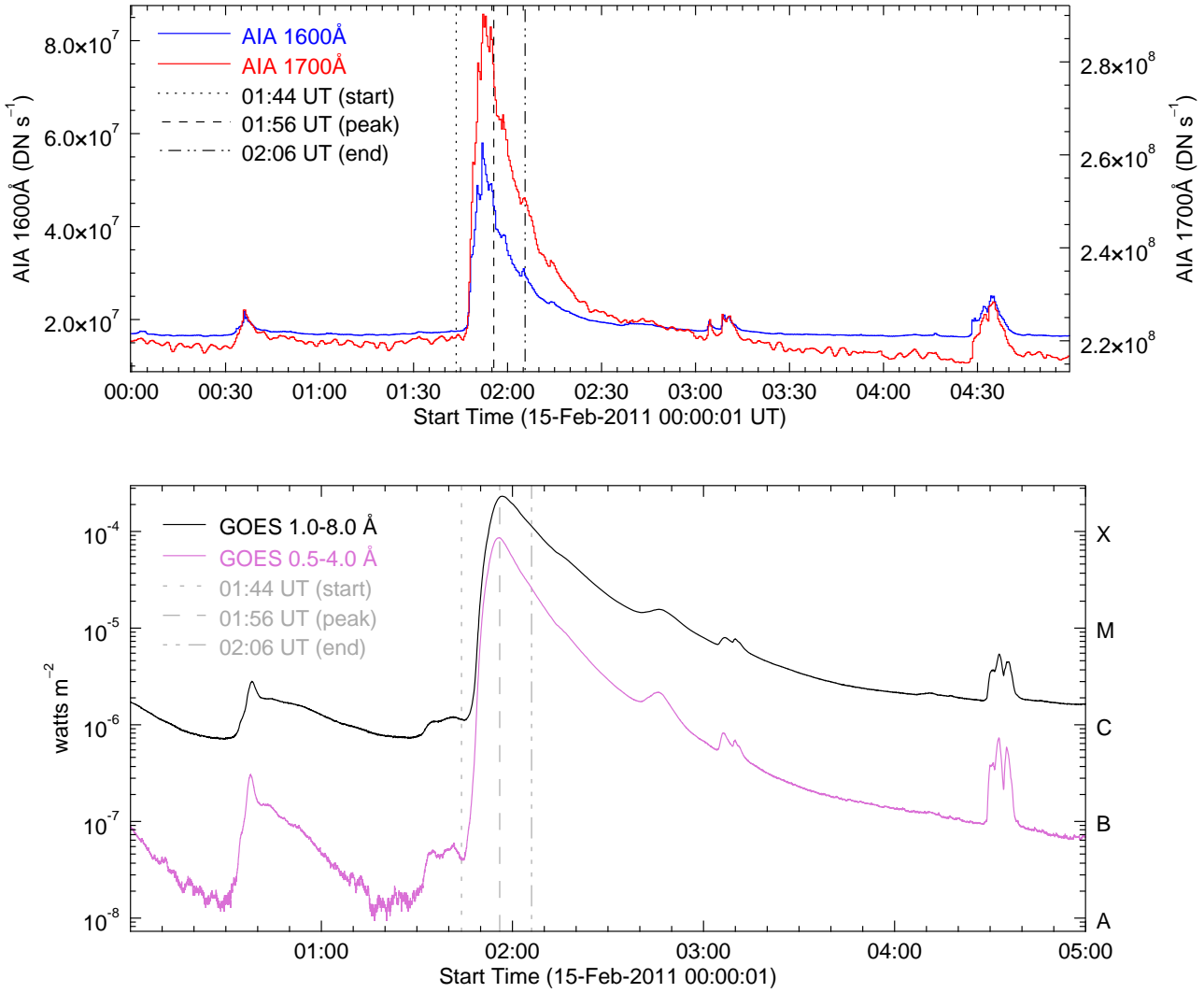


Fig. 1. Top: Light curves of the UV continuum emission from AIA 1600Å (blue curve) and AIA 1700Å (red curve), integrated over the flare region in AR 11158. Bottom: Light curves from *GOES-15* channels 1-8Å (black curve) and 0.5-4Å (pink curve), scaled as log(flux) to enable visibility of the increases during smaller events before and after the main X-flare.

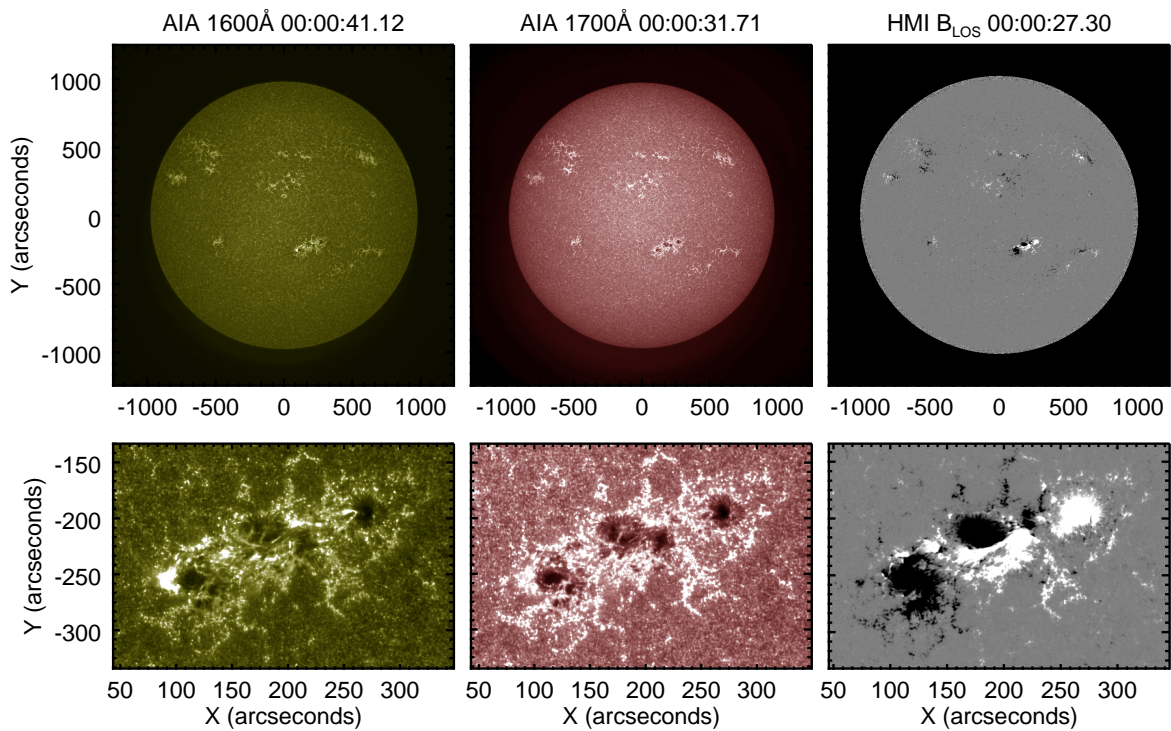


Fig. 2. Images of active region 11158 in AIA 1600Å (left panels), AIA 1700Å (middle panels), and HMI LOS magnetogram (right panels), scaled to ± 300 Gauss. The top panels show the full disk, and the bottom panels show the region used for analysis in this study.

3. ANALYSIS

The technique used to calculate power maps as functions of space and time is similar to that employed by Jackiewicz & Balasubramaniam (2013) and further employed by Monsue et al. (2016). The general method is as follows: For a data set of N images, each power map $P(x, y, t_i)$ is generated by applying a Fourier transform to every pixel at (x, y) in the temporal direction, from t_i to $t_i + T$, where T is the length of the time segment. The power is averaged over a frequency band $\Delta\nu$ of user-defined width, centered on the frequency of interest. This process is repeated at every timestep, for starting times from t_0 to t_{N-T} .

The data set for AR 11158 consisted of $N = 749$ images (5 hours) of AIA observations in each channel. Each time segment T was set to 64 images (~ 25.6 minutes). The value of T was chosen based on a balance between sufficient length to obtain frequencies close to that of the 3-minute period and not so long as to lose information on timescales over which the 3-minute power was previously observed to change. Each Fourier transform was applied without detrending the data since the frequency of interest was well outside the global flare signal. (As a check on this, a Fourier filter was applied with a cutoff period above 400 seconds. The power spectra for the periods of interest did not change.) If a saturated pixel was encountered in any segment t_i to $t_i + T$, it was excluded from the power map for that time segment, and the location (x, y) of that pixel was set to zero.

The frequency bandwidth $\Delta\nu$ was set to 1 mHz centered on $\nu \sim 5.6$ mHz. This is consistent with similar techniques applied in previous studies. For instance, Stangalini et al. (2011) used a 1-mHz frequency bandpass between 4.8 mHz (208.3 seconds) and 5.8 mHz (172.4 seconds) when calculating power maps around 5.6 mHz for the chromosphere and photosphere. Tripathy et al. (2018) also used a band of 1 mHz over 0.1-mHz steps from 1 to 10.5 mHz. Reznikova et al. (2012) used a bandpass of only 0.4 mHz...

With these input parameters, a frequency resolution $\partial\nu$ of ~ 0.65 mHz was obtained. Two frequencies were obtained within $\Delta\nu$ at 5.21 mHz (192.00 seconds) and 5.86 mHz (170.67 seconds).

The average power over $\Delta\nu$ for each unsaturated pixel in time segment T from t_i to $t_i + T$ was taken to be the 3-minute power in each power map. Since only two frequencies were obtained within $\Delta\nu$, and were centered around the frequency of interest, the average was computed without the application of a filter.

Power maps representing the 3-minute power over NOAA AR 11158 in space and time were obtained at every starting point in the time series (up to $N - T$) by applying a Fourier transform to the signal from each pixel, and averaging the power within the 1-mHz frequency bandwidth $\Delta\nu$ centered around 5.6 mHz (3 minutes).

4. RESULTS

4.1. Spatial distribution of oscillatory power

Many of the general patterns in the spatial distribution of 3-minute power were consistent throughout the time series. Figure 3 is presented as an illustrative example, showing post-flare intensity images and corresponding power maps for AIA 1600Å and AIA 1700Å, overlaid with HMI B_{LOS} contours at ± 300 Gauss from the center of the time segment used to produce the power map (around 3:12 UT). Negative polarities are outlined in black and positive polarities are outlined in white.

The location of power enhancement appears to be correlated with intensity, though not all locations of high intensity are accompanied by enhanced power. These locations are also constrained to areas directly around the active region, but do not appear to branch out into the quiescent network/internetwork regions beyond. Power enhancement occurs in relatively *small* regions. A few isolated regions of enhancement covered an area of $\sim 6'' \times 6''$. The 3-minute power appears to be suppressed in most of the areas directly over the umbra.

4.1.1. Correlation with B_{LOS}

In most power maps, the power enhancement is located along the boundaries of magnetic field strength = ± 300 Gauss, which correlates with the outer boundary of the penumbra. (It should be noted that the alignment procedures may have resulted in a slight offset between the channels, in addition to any existing LOS affects.)

4.2. Temporal evolution of oscillatory power

4.2.1. Pre-flare

Figure 4 shows the spatial distribution of 3-minute power for various time segments of interest from 00:00 UT up to 01:44 UT. This period includes a C-class flare that occurred an hour before the X-class flare in AR_2b. A particularly prominent spot emerges in the lower edge of AR_1a and persists until the decay phase of the X-class flare.

4.2.2. During the flare

Figure 5 shows the spatial distribution of 3-minute power for various time segments of interest during the X-class flare. Pixels that saturated were excluded from the maps to improve contrast between the remaining pixels. Bleeding that occurred at the edges of saturated areas could not be excluded since these values started to approach those held by pixels that were not saturated.

Maps (a)-(c) were produced from intensity images that included pre-flare and precursor emission, before the channels began to saturate. They are as close in time as allowed by the instrumental cadence, and there is still a noticeable increase in enhancement in the flare site over AR_1b and AR_2a.

Maps (d)-(f) include emission from the impulsive phase, and maps (g)-(i) include emission from AIA peak emission and onward through the decay phase.

4.2.3. Post-flare

Figure 6 shows the spatial distribution of 3-minute power for various time segments of interest during the X-class flare. There were two small events after the X-class flare.

4.2.4. Discrete wavelet analysis

The technique described in §3 was applied to the integrated flux from AR 11158 at discrete intervals of $T = 64$ images with no overlap (i.e. for start time t_0 , then $t_1 = t_0 + T$, etc.). This provided a “quick and dirty” way to compare the spectral power at a range of frequencies. This method produces similar results to those obtained with wavelet analysis, though at lower resulting frequency and time resolution. The results are shown in Figure 8 for frequencies between 2.5 and 20.0 mHz (400 and 50 seconds, respectively). The central frequency $\nu_c = 5.56$ mHz and the frequency bandpass $\Delta\nu$ at 5 and 6 mHz are marked by the horizontal dashed lines. The power at all frequencies appears to be enhanced during the X-flare compared to their non-flaring power before and after. During the small events before and after the flare, the power at lower frequencies is enhanced, but the power at higher frequencies is suppressed relative to the same frequencies for adjacent time segments.

At all points in time when power enhancement occurs for any frequency, there appears to be a correlation with flux increase.

The location of these enhancements does not move across the AR. Rather, it remains in one place until it fades away. One of the most prominent locations of enhanced power occurs before the flare at the bottom of the leading sunspot in the northern pair. The change in location with time of both flare intensity and 3-minute power implies that the source of the beam of non-thermal particles changes as well.

3-minute oscillations are interpreted as slow, propagating magnetoacoustic waves, which have a characteristic excitation mechanism and damping rate, depending on the local plasma conditions where they originate. The timescales over which the oscillatory power is expected to change depends on the nature of the oscillations themselves, or maybe the cooling rate of the plasma. The expected timescales would depend on the cooling rate of the plasma (images) and the damping time/mechanisms of the 3-minute oscillations.

4.2.5. AIA formation heights/temperatures

The evolution of the 3-minute power with time was calculated from the power maps by summing over x and y in each map $P(x, y, t_i)$, and taking the total to be the

3-minute power of the active region during each time segment. This is shown in Figure 7. Each point is plotted as a function of the center of the time segment over which the Fourier transform was applied to obtain that point. The axis labelled $T = 64$ shows the scale for this length of time.

Power as a function of time obtained from total flux and power maps is shown to check for possible contradictions between the two. Integrating flux over the AR before applying the Fourier transform has the potential effect of reducing or canceling signal from pixels whose intensity variations are out of phase.

The reason for the apparent periodicity in the plots of 3-minute power with time is unclear. The calculations were repeated for power centered on the 5-minute period and the 2-minute period, and resulted in the same trend, with the additional observation that the length of the central period scaled with the period in the plot of power vs. time. This pattern is attributed to computational effects.

The amplitude of the small-scale variations in 3-minute power is higher for AIA 1700Å almost everywhere with the exception of the main phase of the X-class flare.

When both plots are normalized between 0.0 and 1.0, the variation in power is higher from AIA 1700 almost everywhere except the main phase of the X-class flare, when the power from 1600 is slightly higher.

The power from AIA 1700 is higher than AIA 1600 by 1000 counts at all points throughout the time series. Compared to 1700Å, the 1600Å 3-minute power appears to increase more (relative to its own minimum) and at a faster rate. The standard deviation for $P(t)$ from integrated flux for 1600Å is 4.9×10^4 , and for 1700Å is 2.7×10^4 .

If the emission from AIA 1600Å originates from a higher location in the atmosphere than the 1700Å emission, a possible explanation for the higher, sharper increase is that the energy from the non-thermal particle beam dissipates as it travels through deeper layers of the chromosphere. Because AIA 1700 originates from a deeper layer, it is probably more dense as well, which would cause the plasma to cool at a slower rate. If the 3-minute power originated from the transition region rather than the upper photosphere, this may coincide with the levitation of hot chromospheric plasma upward into post-flare loops. Although the emission from AIA 1700Å is generally thought to originate in lower formation heights than emission from 1600Å, the latter spans a broader temperature range, and contains emission from C IV line. Determination of the AIA 1600Å formation height is more complicated during flares because the C IV is more likely to be contributing to the signal, and both channels may be sampling at deeper layers than they are thought to during non-flaring times.

The persistence of the 3-minute power toward the end of the gradual phase in AIA 1700Å is consistent with the

results of the wavelet analysis carried out by Milligan et al. (2017).

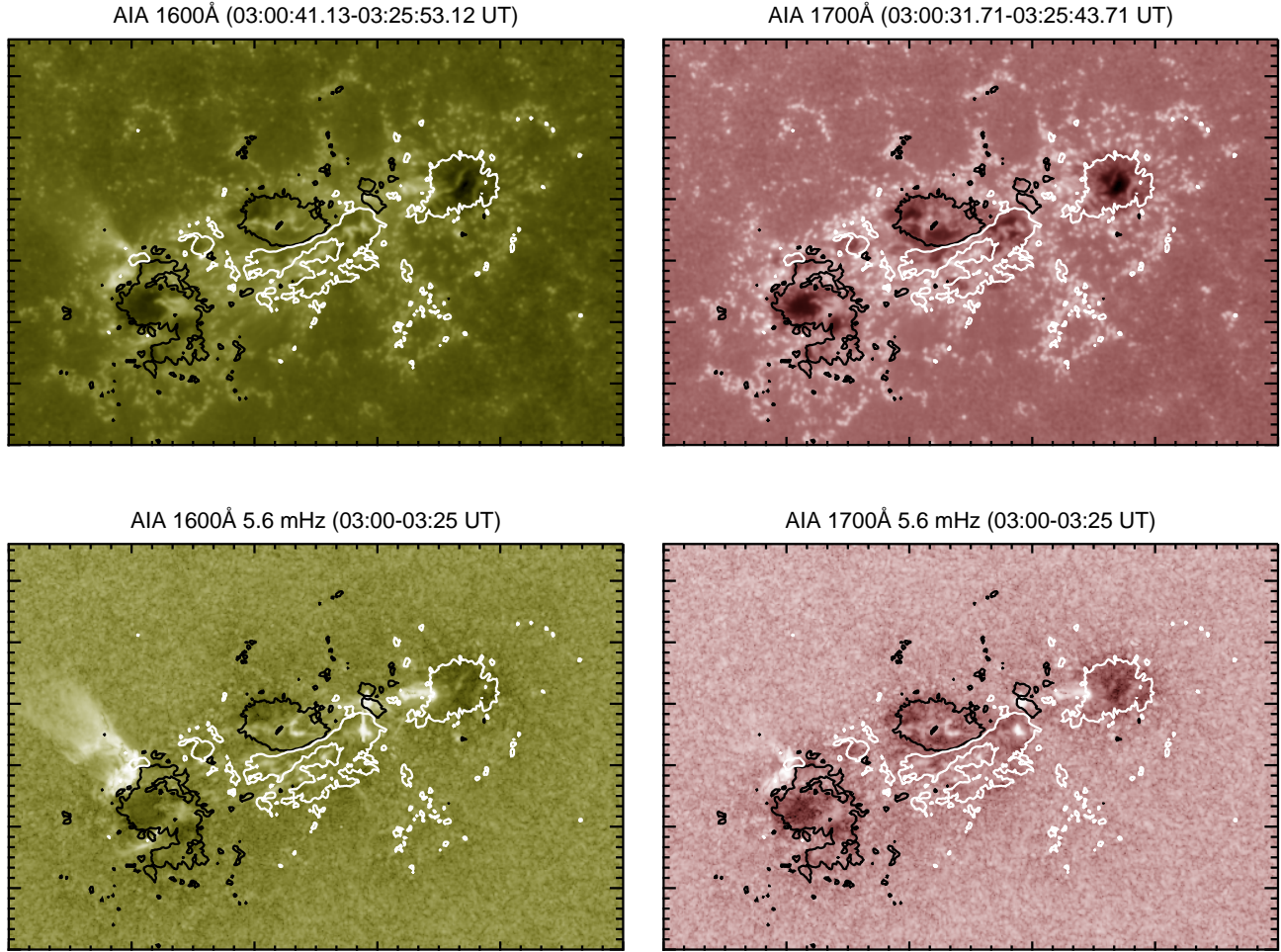


Fig. 3. Top row: Post-flare images, shown as a composite product over the time range shown, overlaid with contours showing the approximate location of the B_{LOS} at ±300 Gauss. Bottom rows: Spatial distribution of 3-minute power, obtained by applying a pixel-by-pixel Fourier transform over the images included in the top row. The left column shows results from AIA 1600Å, and the right column shows results from AIA 1700Å. White and black contours represent positive and negative polarity, respectively.

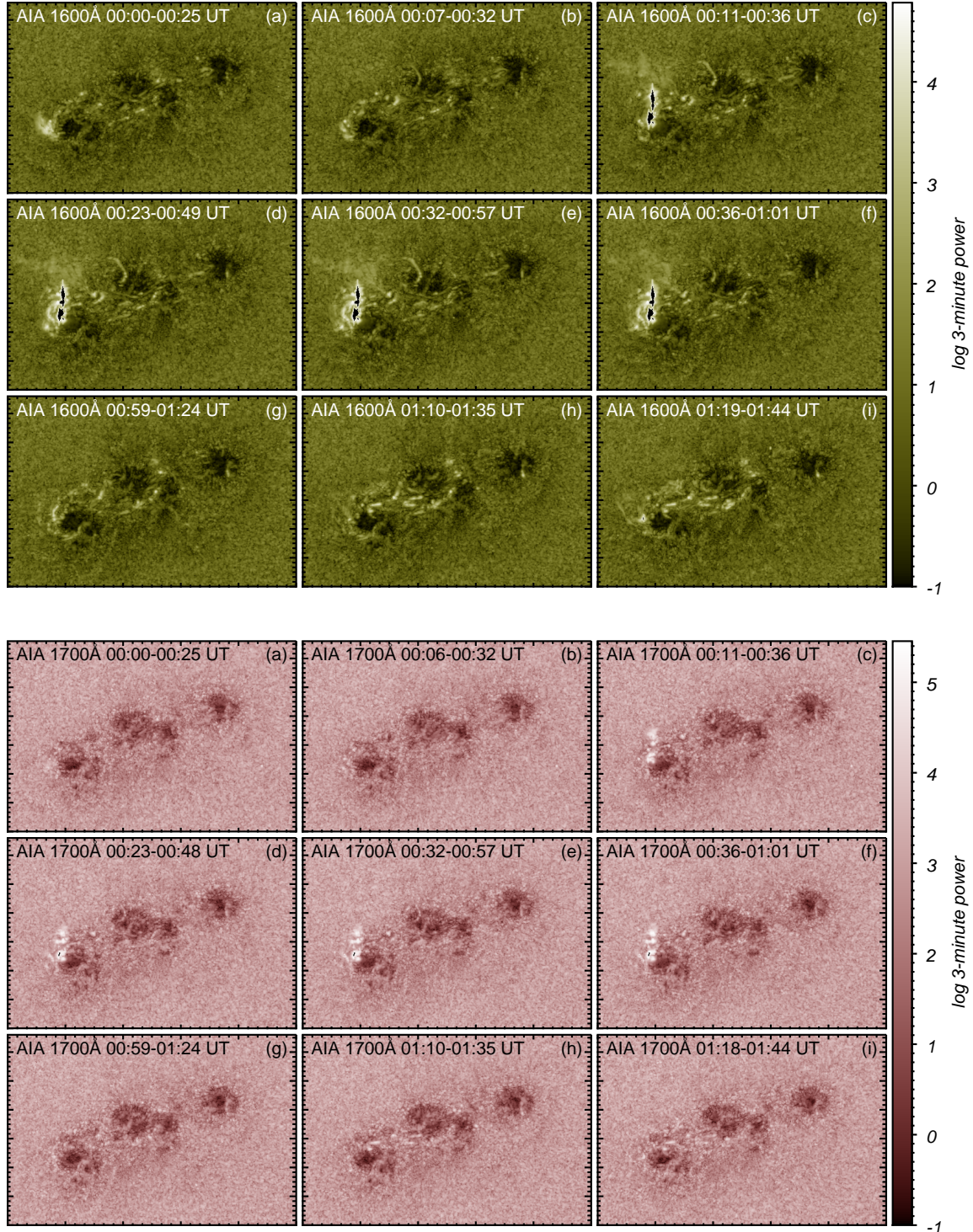


Fig. 4. Spatial distribution of 3-minute power before the X-class flare, in log scale to bridge large contrasts. Locations whose time segment included saturated pixels were set to zero.

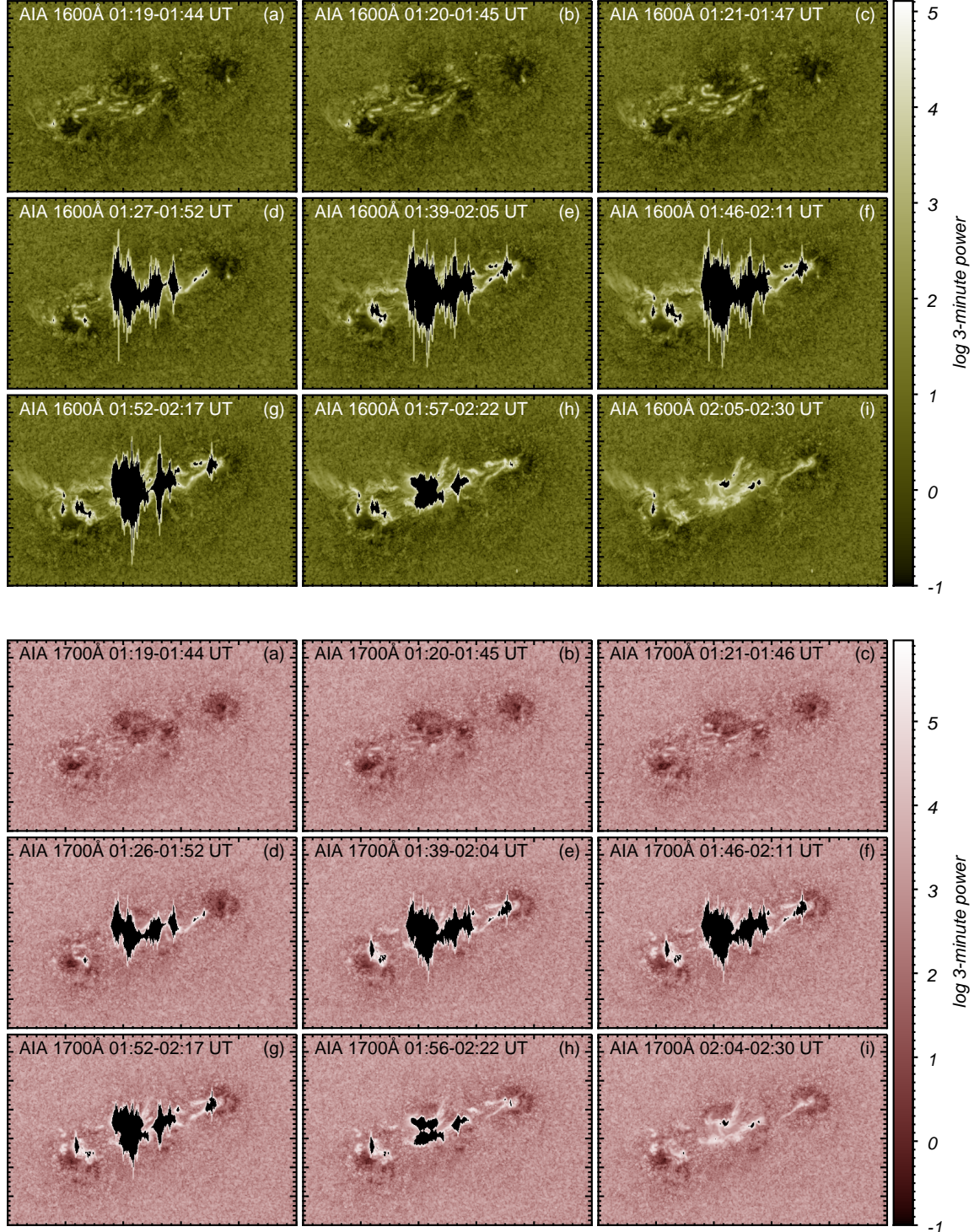


Fig. 5. Spatial distribution of 3-minute power during the X-class flare, in log scale to bridge large contrasts. Locations whose time segment included saturated pixels were set to zero.

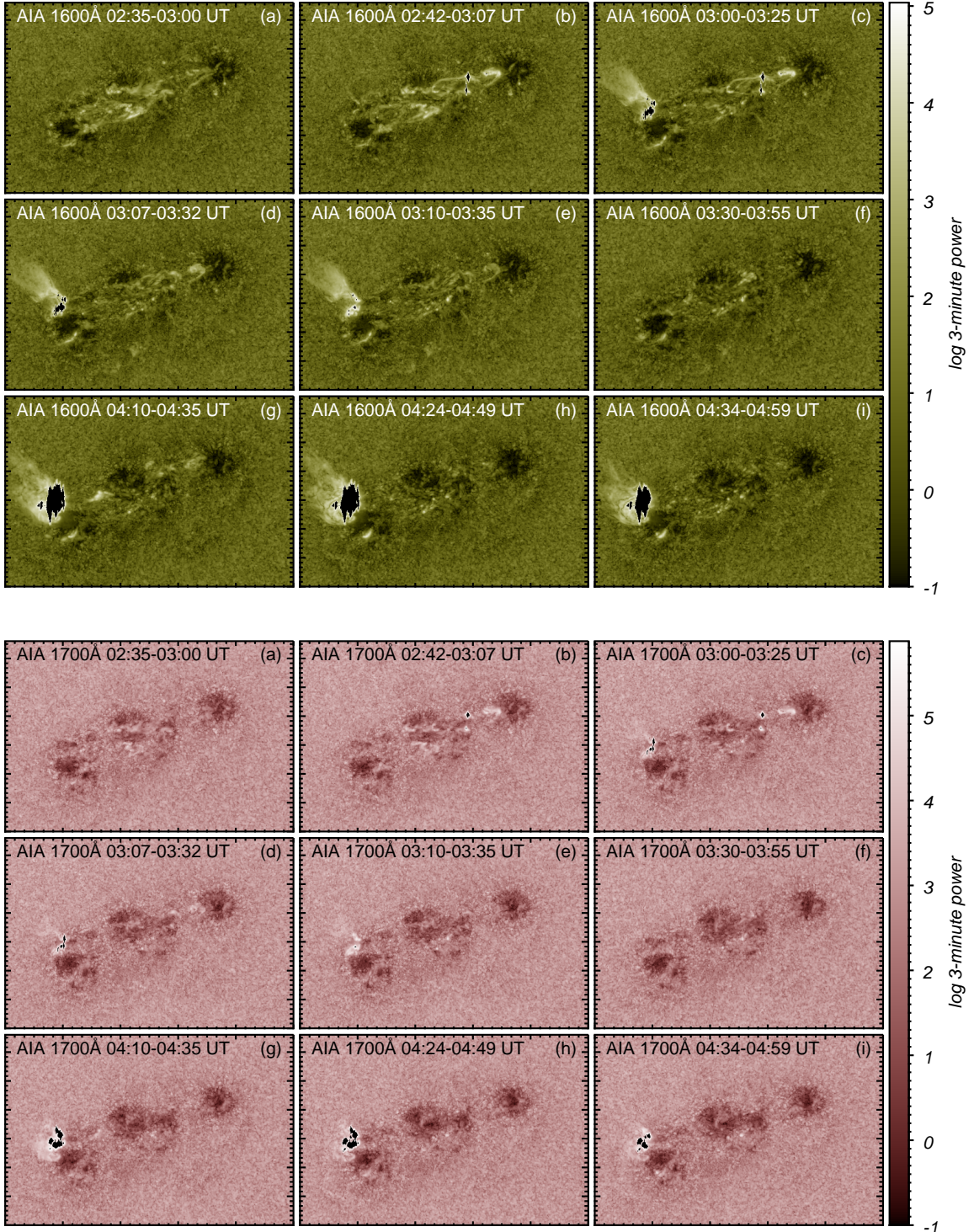


Fig. 6. Spatial distribution of 3-minute power after the X-class flare, in log scale to bridge large contrasts. Locations whose time segment included saturated pixels were set to zero.

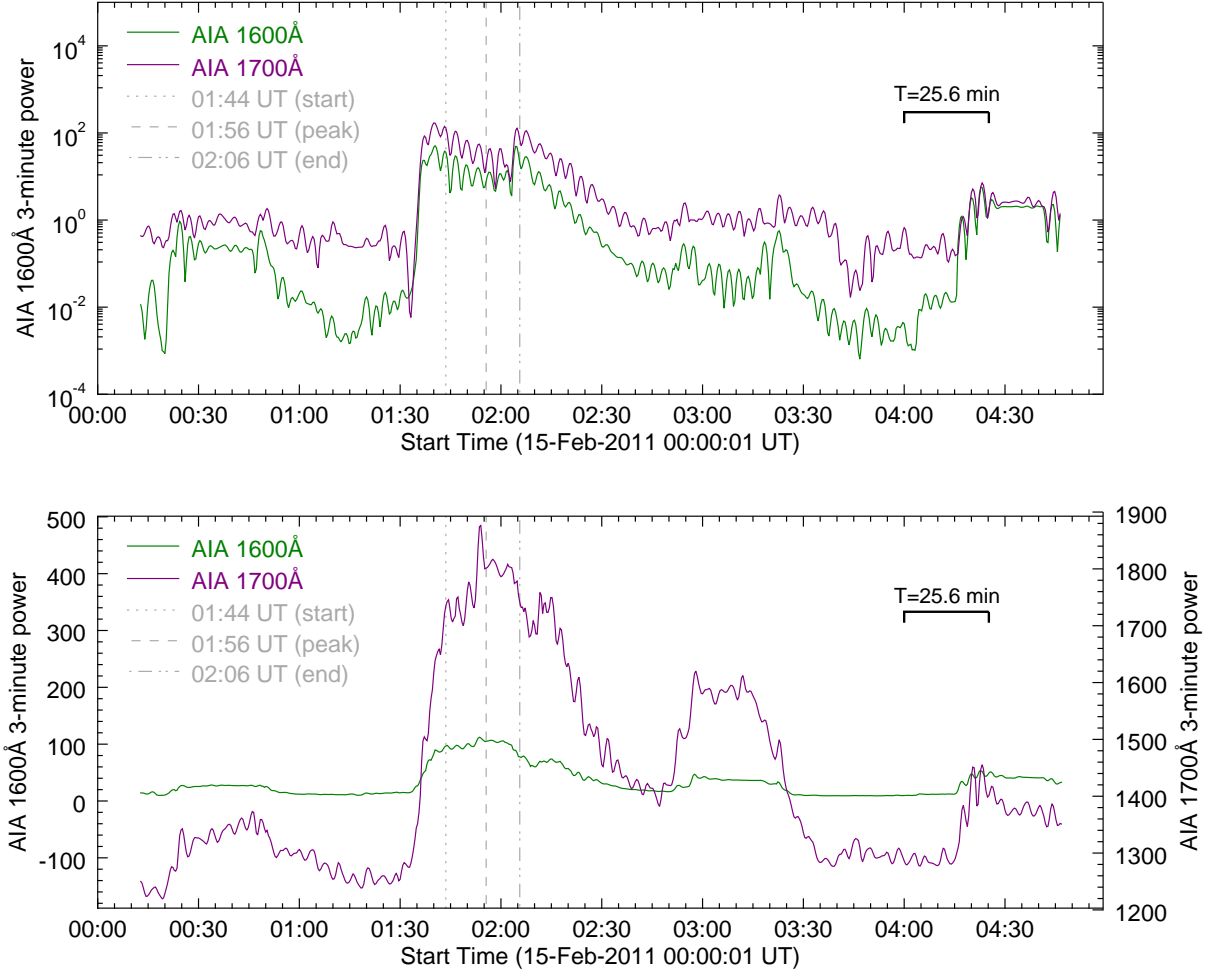


Fig. 7. Temporal evolution of the 3-minute power $P(t)$ in AIA 1600 \AA (green curve) and AIA 1700 \AA (purple curve). Top: $P(t)$ obtained by applying a Fourier transform to the integrated flux from AR 11158. Bottom: $P(t)$ per unsaturated pixel, obtained by summing over power maps. Each point in time is plotted as a function of the center of the time segment over which the Fourier transform was applied to obtain the power map over which the point was summed. The vertical dashed lines mark the GOES start, peak, and end times of the flare at 01:44, 01:56, and 02:06 UT, respectively.

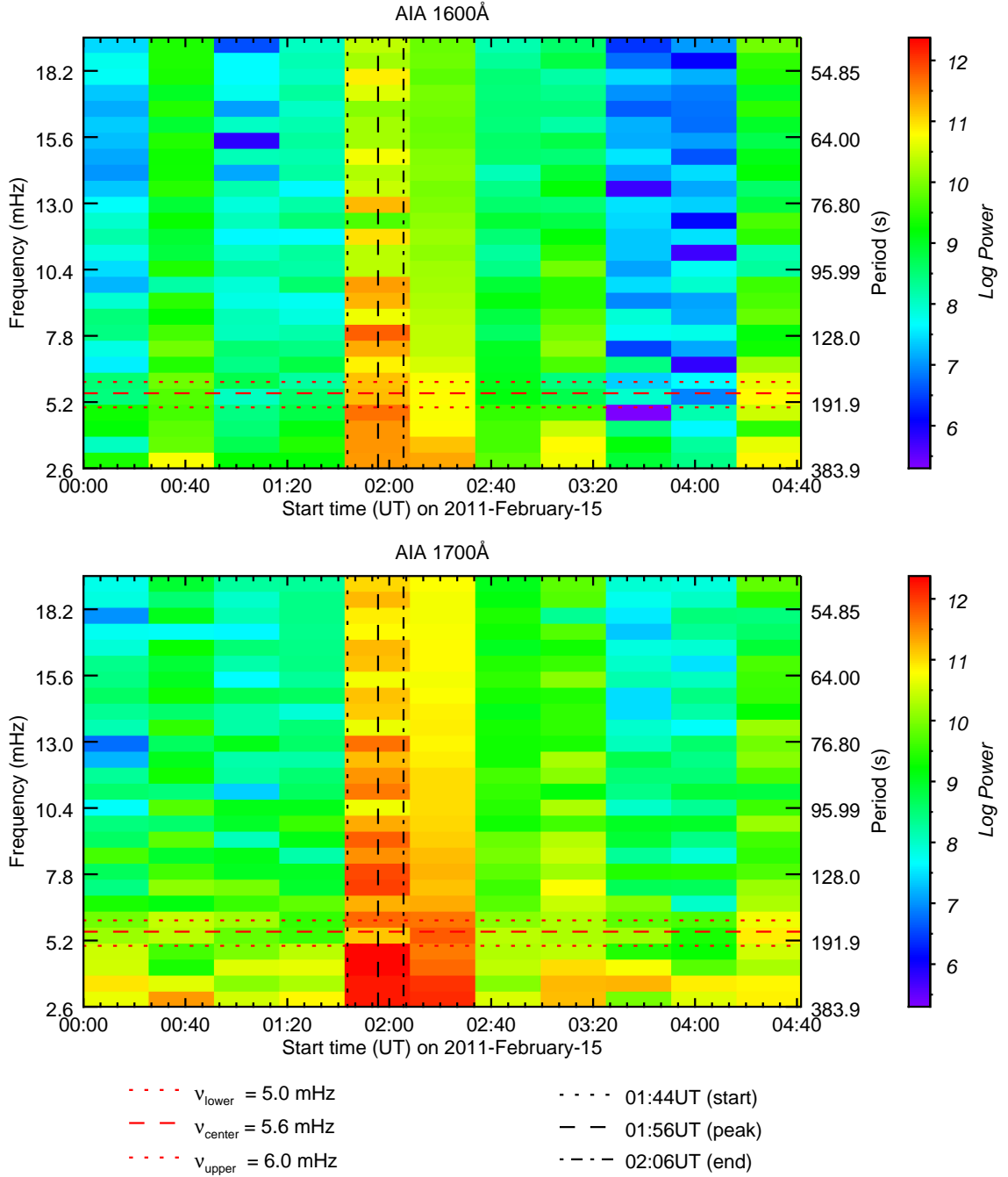


Fig. 8. Time-frequency power plots from AIA 1600Å (top panel) and AIA 1700Å (bottom panel), obtained by applying a Fourier transform to integrated emission from NOAA AR 11158 in discrete time increments of 64 frames (~ 25.6 minutes) each. The dashed horizontal line marks the central frequency ν_c at ~ 5.6 mHz, corresponding to a period of 3 minutes. The dotted horizontal lines on either side of ν_c mark the edges of the frequency bandpass $\Delta\nu = 1$ mHz. The vertical lines mark the flare, start, peak, and end times as determined by *GOES*. The power is scaled logarithmically and over the same range in both channels.

5. DISCUSSION

The small periodicities can be difficult to extract from the global lightcurve ([Van Doorsselaere et al. 2016](#)).

The concentration of power enhancement in small areas located in the vicinity of sunspot umbrae suggests that [these small areas of the chromosphere are responding directly to the injection of energy by a beam of non-thermal particles. Umbral brightenings/dots?](#)

If the location of power enhancement does reveal sites of energy injection, then [it remains possible that changes in energy source coincides with the location of power changes.](#)

[Compare my results from integrated emission to others. Then compare my results from spatially resolved data. Does it contradict those from integrated emission? Do the relative changes in the two AIA channels match?](#)

Almost all events before and after the main X-class flare occurred in AR_2b, including briefly at the beginning of the time series.

6. CONCLUSIONS AND FUTURE WORK

In this work, we have used spatially resolved data from SDO/AIA and SDO/HMI to constrain the location and time that enhancement in the power of the 3-minute oscillations occurred before, during, and after an X-class flare. Results support the theory of energy injection by acceleration of non-thermal particles, and the response of the chromosphere to this injection in thermal wavelengths.

The preliminary results of this work support the following conclusions:

1. The enhancement of 3-minute power is concentrated in small areas that coincide with locations of enhanced flare emission. This supports the theory of energy injection by a beam of accelerated non-thermal particles. It also shows that the chromospheric plasma does not oscillate globally as one body across the active region.
2. The 3-minute power changes more for AIA 1600Å than for 1700Å, which suggests that the 1600Å emission originates from higher layers.

There are several possibilities for the continuation of this work.

Here we focused on the oscillations centered around the 3-minute period, but the inclusion of other periods in the typical range of QPPs periods will be helpful to see how the behavior of the 3-minute oscillations differs from others, to set it apart from the range of frequencies excited due to energy injection.

Since several of the data images saturated during the main phase of the flare, spatial information cannot be obtained at the core location of the flare. It may be worthwhile to apply these methods to a less powerful flare.

The temporal behavior of oscillations during the main flare remains inconclusive due to the necessary balance between temporal and frequency resolution. Techniques to improve temporal resolution, such as the standard wavelet analysis presented by [Torrence & Compo \(1998\)](#), will allow study of chromospheric behavior on timescales comparable to those over which flare dynamics are known to occur.

Indeed, the timescales over which the oscillatory power changed in the study by [Milligan et al. \(2017\)](#) were much shorter than the sample time length used here. The choice of T was necessary to obtain sufficient frequency resolution with the techniques utilized here, at the expense of temporal resolution.

REFERENCES

- Awasthi, A. K., Rudawy, P., Falewicz, R., Berlicki, A., & Liu, R. 2018, ApJ, 858, 98, doi: [10.3847/1538-4357/aabd76](https://doi.org/10.3847/1538-4357/aabd76)
- Brosius, J. W., & Daw, A. N. 2015, ApJ, 810, 45, doi: [10.1088/0004-637X/810/1/45](https://doi.org/10.1088/0004-637X/810/1/45)
- Chae, J., & Goode, P. R. 2015, ApJ, 808, 118, doi: [10.1088/0004-637X/808/2/118](https://doi.org/10.1088/0004-637X/808/2/118)
- De Pontieu, B., Title, A. M., Lemen, J. R., et al. 2014, SoPh, 289, 2733, doi: [10.1007/s11207-014-0485-y](https://doi.org/10.1007/s11207-014-0485-y)
- Fletcher, L., Hannah, I. G., Hudson, H. S., & Innes, D. E. 2013, ApJ, 771, 104, doi: [10.1088/0004-637X/771/2/104](https://doi.org/10.1088/0004-637X/771/2/104)
- Inglis, A. R., Ireland, J., & Dominique, M. 2015, ApJ, 798, 108, doi: [10.1088/0004-637X/798/2/108](https://doi.org/10.1088/0004-637X/798/2/108)
- Jackiewicz, J., & Balasubramaniam, K. S. 2013, ApJ, 765, 15, doi: [10.1088/0004-637X/765/1/15](https://doi.org/10.1088/0004-637X/765/1/15)
- Kumar, B., & Ravindra, B. 2006, Journal of Astrophysics and Astronomy, 27, 425, doi: [10.1007/BF02709368](https://doi.org/10.1007/BF02709368)
- Kwak, H., Chae, J., Song, D., et al. 2016, ApJL, 821, L30, doi: [10.3847/2041-8205/821/2/L30](https://doi.org/10.3847/2041-8205/821/2/L30)
- Lemen, J. R., Title, A. M., Akin, D. J., et al. 2012, SoPh, 275, 17, doi: [10.1007/s11207-011-9776-8](https://doi.org/10.1007/s11207-011-9776-8)
- McAteer, R. T. J., Gallagher, P. T., Bloomfield, D. S., et al. 2004, ApJ, 602, 436, doi: [10.1086/380835](https://doi.org/10.1086/380835)
- McAteer, R. T. J., Gallagher, P. T., Williams, D. R., et al. 2003, ApJ, 587, 806, doi: [10.1086/368304](https://doi.org/10.1086/368304)
- Milligan, R. O., Fleck, B., Ireland, J., Fletcher, L., & Dennis, B. R. 2017, ArXiv e-prints. <https://arxiv.org/abs/1709.09037>
- Monsue, T., Hill, F., & Stassun, K. G. 2016, AJ, 152, 81, doi: [10.3847/0004-6256/152/4/81](https://doi.org/10.3847/0004-6256/152/4/81)
- Nakariakov, V. M., & Melnikov, V. F. 2009, SSRv, 149, 119, doi: [10.1007/s11214-009-9536-3](https://doi.org/10.1007/s11214-009-9536-3)
- Pesnell, W. D., Thompson, B. J., & Chamberlin, P. C. 2012, SoPh, 275, 3, doi: [10.1007/s11207-011-9841-3](https://doi.org/10.1007/s11207-011-9841-3)
- Reznikova, V. E., Shibasaki, K., Sych, R. A., & Nakariakov, V. M. 2012, ApJ, 746, 119, doi: [10.1088/0004-637X/746/2/119](https://doi.org/10.1088/0004-637X/746/2/119)
- Scherrer, P. H., Schou, J., Bush, R. I., et al. 2012, SoPh, 275, 207, doi: [10.1007/s11207-011-9834-2](https://doi.org/10.1007/s11207-011-9834-2)
- Schou, J., Scherrer, P. H., Bush, R. I., et al. 2012, SoPh, 275, 229, doi: [10.1007/s11207-011-9842-2](https://doi.org/10.1007/s11207-011-9842-2)
- Stangalini, M., Del Moro, D., Berrilli, F., & Jefferies, S. M. 2011, A&A, 534, A65, doi: [10.1051/0004-6361/201117356](https://doi.org/10.1051/0004-6361/201117356)
- Sutmann, G., Musielak, Z. E., & Ulmschneider, P. 1998, A&A, 340, 556
- Sutmann, G., & Ulmschneider, P. 1995a, A&A, 294, 232
- . 1995b, A&A, 294, 241
- Sych, R., Nakariakov, V. M., Karlicky, M., & Anfinogentov, S. 2009, A&A, 505, 791, doi: [10.1051/0004-6361/200912132](https://doi.org/10.1051/0004-6361/200912132)
- Torrence, C., & Compo, G. P. 1998, Bulletin of the American Meteorological Society, 79, 61
- Tripathy, S. C., Jain, K., Kholikov, S., et al. 2018, Advances in Space Research, 61, 691, doi: [10.1016/j.asr.2017.10.033](https://doi.org/10.1016/j.asr.2017.10.033)
- Van Doorsselaere, T., Kupriyanova, E. G., & Yuan, D. 2016, SoPh, 291, 3143, doi: [10.1007/s11207-016-0977-z](https://doi.org/10.1007/s11207-016-0977-z)
- Viereck, R., Hanser, F., Wise, J., et al. 2007, in Proc. SPIE, Vol. 6689, Solar Physics and Space Weather Instrumentation II, 66890K